SOFT ROBOTICS
Volume 11, Number 5, 2024

DOI: 10.1089/soro.2023.0120

SoRo
Soft Robotics



***ORIGINAL ARTICLE***

# Stiffness Change for Reconfiguration of Inflated Beam Robots

Brian H. Do, Shuai Wu, Ruike Renee Zhao, and Allison M. Okamura



***Abstract***

Active control of the shape of soft robots is challenging. Despite having an infinite number of *passive* degrees of freedom (DOFs), soft robots typically only have a few *actively controllable* DOFs, limited by the number of degrees of actuation (DOAs). The complexity of actuators restricts the number of DOAs that can be incorporated into soft robots. Active shape control is further complicated by the buckling of soft robots under compressive forces; this is particularly challenging for compliant continuum robots due to their long aspect ratios. In this study, we show how variable stiffness enables shape control of soft robots by addressing these challenges. Dynamically changing the stiffness of sections along a compliant continuum robot selectively ''activates'' discrete joints. By changing which joints are activated, the output of a single actuator can be reconfigured to actively control many different joints, thus decoupling the number of controllable DOFs from the number of DOAs. We demonstrate embedded positive pressure layer jamming as a simple method for stiffness change in inflated beam robots, its compatibility with growing robots, and its use as an ''activating'' technology. We experimentally characterize the stiffness change in a growing inflated beam robot and present finite element models that serve as guides for robot design and fabrication. We fabricate a multisegment everting inflated beam robot and demonstrate how stiffness change is compatible with growth through tip eversion, enables an increase in workspace, and achieves new actuation patterns not possible without stiffening.

**Keywords:** variable stiffness, layer jamming, inflated beam robot, growing robot, shape change, soft robotics

## Introduction

The compliance of soft robots gives them an infinite number of passive degrees of freedom (DOFs). This enables soft robots to adapt to environmental uncertainty even with simple mechanical design, a feature referred to as embodied intelligence.[1] These soft robots can be low inertia and inherently safer for interaction tasks with people and objects. They offer the potential to expand the capabilities of robots from the traditional manipulation, inspection, and navigation tasks where rigid robots dominate to new tasks such as physical human–robot interaction.

Compliance also makes active control of soft robots challenging. Typically, few of a soft robot's DOFs are controlled by its actuators. This limits the ability of soft robots to vary their morphology on-demand. Using more actuators can increase the number of actively controllable DOFs but also increases the complexity, weight, and cost of soft robots. Ultimately, this approach is difficult to scale, with the fabrication and control complexity being limiting factors.

Department of Mechanical Engineering, Stanford University, Stanford, California, USA.
A preprint of this article can be found on ArXiv at 10.48550/arXiv.2307.03247.

The traditional paradigm in robotics has been to achieve high dexterity through the use of many actuators, each controlling one specific DOF. For example, in the field of robot manipulation, many fully actuated hand designs exist with an actuator for each finger joint.[2] In the field of inflated beam robots, past inflatable robotic arms have relied either on actuators located at the joints[3] or cables running from each joint to a base.[4,5] However, this often results in expensive, complicated, or bulky designs, which require complex sensing and control.

Designing robots to be underactuated, such as by using passive joints, can reduce the number of actuators used. However, with underactuation, there is a trade-off between the embodied intelligence of robots and their controllability. Multiple DOFs are now coupled to a given actuator, and this mapping between actuators and the set of DOFs these actuators are coupled to cannot be changed after the design stage.

Variable stiffness represents another approach to change robot output shape. Biological organisms utilize variable stiffness to *change* their shape by adapting their morphology. For example, octopuses create virtual joints in their arms by stiffening them during reaching movements,[6] and elephants actively stiffen their trunks during grasping to create a virtual joint whose location depends on the size of the object they are grasping.[6]

Although a variety of approaches have been proposed for stiffness control in soft robots, most of these focus on stiffness change from low to high stiffness states to *maintain* their shape. For example, in grasping, variable stiffness fingers can initially be low stiffness to enable compliant interactions with an object during grasp acquisition, and once the object is acquired, transition to high stiffness to hold the object without the fingers deforming and yielding, thus increasing their maximum bearing capacity.[7–9] Here, stiffness change is decoupled from actuation and is used for shape locking once a desired shape has already been reached.

However, stiffness can be used to modulate actuator outputs to yield more complex shape outputs. Past approaches have investigated either robots with global stiffness change[10–12] or robots discretized into different segments each with their own independent stiffness and actuation systems.[13] Neither of these approaches varies the robot kinematics or enables a high number of controllable DOFs with fewer degrees of actuation (DOAs), that is, the number of independent actuators used to control a system's DOFs.

In this study, we explore how stiffness change enables reconfiguration of soft inflated beam robots by modulating actuator output and varying robot kinematics. Inflated beam robots are characterized by their use of internal gas pressure as the supporting element.[14–16] Similar to other continuum robots, inflated beam robots are attractive for human–robot interaction due to their low inertia and have long thin-aspect ratios.[15]

We focus on the class of inflated beam robots capable of pressure-driven tip eversion, often referred to as ''vine'' robots. These everting robots use a flexible but inextensible tube as a pneumatic backbone and ''grow'' by pneumatically everting material at their tip, enabling these robots to be stored compactly and achieve high extension ratios.[17–19] These robots have previously been investigated for manipulation,[20] navigation,[21,22] and search and rescue.[23]

Building on our initial explorations,[24,25] we show how stiffness change can be leveraged for active reconfiguration of soft robots through the design, modeling, and fabrication of an everting inflated beam robot with distributed variable stiffness. Stiffness is used to modify the output of actuators, enabling a single actuator to selectively control multiple independent DOFs and which joint(s) are bent, enabling us to increase dexterity without increasing the number of actuators.

Transforming the output of a few complex actuators enables greater adaptive morphing of high-DOF robots. We achieve stiffness change through layer jamming, including positive pressure layer jamming, and characterize this stiffness change both experimentally and in simulation. Finally, we present demonstrations and investigate how stiffness change expands robot workspace and demonstrate complex shape change in free space.

## Materials and Methods

### *Design concept*

Figure 1A illustrates how stiffness change enables reconfiguration in inflated beam robots. If we discretize the inflated beam robot into sections, each of which is independently stiffened, that patterned stiffness enables bending at specified points. An inherent property of inflated beam robots is that, given a sufficient load, they will undergo either axial or transverse buckling.[26] The force required to induce buckling in an inflated beam is a function of the material properties of its membrane.

In the case where the skin of the robot is sufficiently stiff, the robot will remain straight, as Figure 1A (i) shows. However, if we reduce the membrane stiffness of one of the sections, we can induce bending, as Figure 1A (ii) shows. In this postbuckled state, a local kink is formed at the interface between stiffened and nonstiffened sections, enabling bending.[8] Bends at these points behave analogously to rotations of revolute joints. Thus, stiffness change enables the creation of specific ''revolute joints'' in an otherwise continuum structure.

Joints are formed at specified locations by selectively stiffening all sections where bending is not desired. Afterward, these bends are locked in place by stiffening the bent sections. This process of expressing which joints are active through stiffening and bending, and then locking bends in place, is repeated to produce a desired final shape. Furthermore, multiple bends can be formed simultaneously, with the sequence and magnitude of bending tuned by the stiffness of each section. By making one section less stiff than another section, we induce more bending in the former. Unstiffening all sections resets the robot configuration.

The conventional design paradigm in robotics is to design a robot with a set number of DOFs and directly control each DOF with its own actuator. In such fully actuated systems, there is a fixed one-to-one mapping between DOFs and DOAs. As a consequence, the number of DOFs equals the number of DOAs, and increasing the number of controllable DOFs requires a corresponding increase in the number of actuators. The number of actuators thus becomes a limiting factor to having a high degree-of-freedom rigid or soft robot. We use stiffness change as a method to enable a high number of DOFs, each directly controllable, with a lower number of DOAs.

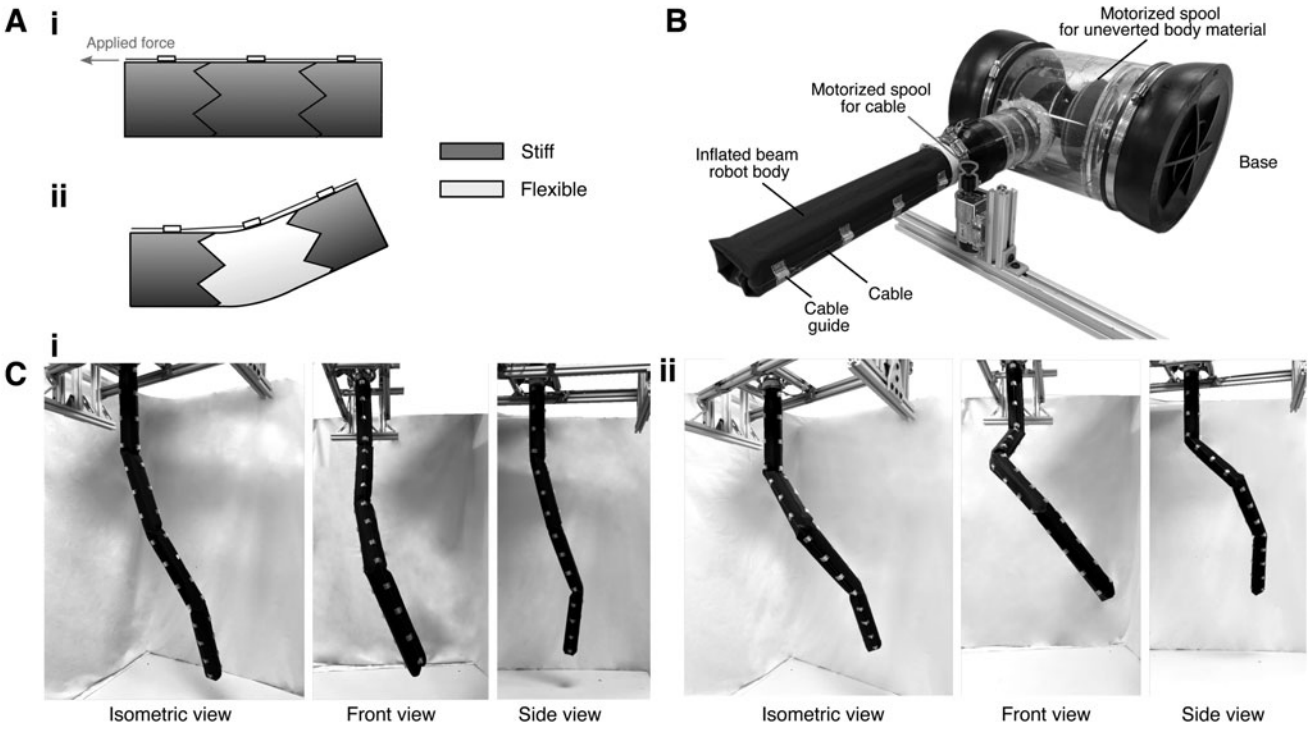


**FIG. 1.** Overview of stiffening vine robot. **(A)** Schematic of a continuum robot discretized into sections, which can be stiff or flexible. In our everting inflated beam robot, stiffening is from layer jamming. (i) Jammed sections are able to resist higher applied forces. (ii) By unjamming a section and then pulling a cable, the inflated beam locally buckles at the interface between stiff and flexible sections, causing the overall beam to bend. This bend acts like a revolute joint. **(B)** Stand-alone variable stiffness vine robot system. The inflated beam of the vine robot grows from a stationary base that stores the uneverted body material. The robot is actuated by motorized cables that connect to motorized spools at the base. **(C)** Vine robot in free space actuated in two different configurations.



As illustrated in Figure 1A, stiffening serves as an ''activator'' to modify the mapping between a given DOA and DOFs.[25,27] An activator does no work on its own but alters an actuator's output. By using a large number of simple activators that modify the output of a few complex actuators, robots can use fewer actuators while retaining complex shape change abilities. We use this actuator-activator paradigm to develop a growing inflated beam robot with dynamically reconfigurable discrete joints.

### *Body design for activation*

Principles. Stiffness change for everting inflated beam robots is subject to a unique constraint: eversion. Any method for stiffness change must be compatible with pressure-driven eversion. During eversion, material undergoes very high curvature at the tip of the robot. Stiffening mechanisms must be able to accommodate this high curvature. Furthermore, as a result of eversion, robots may grow to meters in length, so any stiffness change method should scale to long lengths.

Roboticists have investigated several approaches for stiffness change, such as by inducing a physical change to a material's state, such as with low melting point alloys[28,29] or phase changing alloys.[30] One challenge of these approaches is their slow transition between states.

In this study, we use jamming for stiffening. Jamming is a structural stiffening method in which a pressure difference between particles,[27,31] layers,[32] or fibers[33] results in the bulk structure behaving cohesively, resulting in a state transition from ''flexible'' (unjammed) to ''stiff'' (jammed); this phase transition occurs within seconds. Varying the pressure difference tunes the stiffness, and once the stiffness is set, no energy is required to maintain it.

The particular jamming approach we use is layer jamming. Layer jamming has a thin form factor, a very high stiffness change, and lower volume compared with other jamming techniques. This enables compatibility with tip eversion. Traditional jamming has relied on a vacuum source to generate negative pressure to produce the requisite pressure difference. We also achieve layer jamming without a vacuum source by utilizing the pressure difference between the inflated robot internal pressure and atmospheric pressure.[12,25]

Design overview. Figure 2 shows a schematic of our everting inflated beam robot with distributed variable stiffness. The main body is a tube of material, which is initially inverted. Uneverted material is pulled through the inside of the robot before being everted at the tip. The robot skin is composed of two walls, and the space between these inner and outer walls forms pouches where the jamming layers are located. The robot is discretized into sections, each consisting of a pouch running circumferentially around the robot and containing 6 stacks of paper, with 15 layers each; the layer stacks are described in more detail in Fabrication section. We actuate the robot using tendons and stoppers that run along the length of the robot.

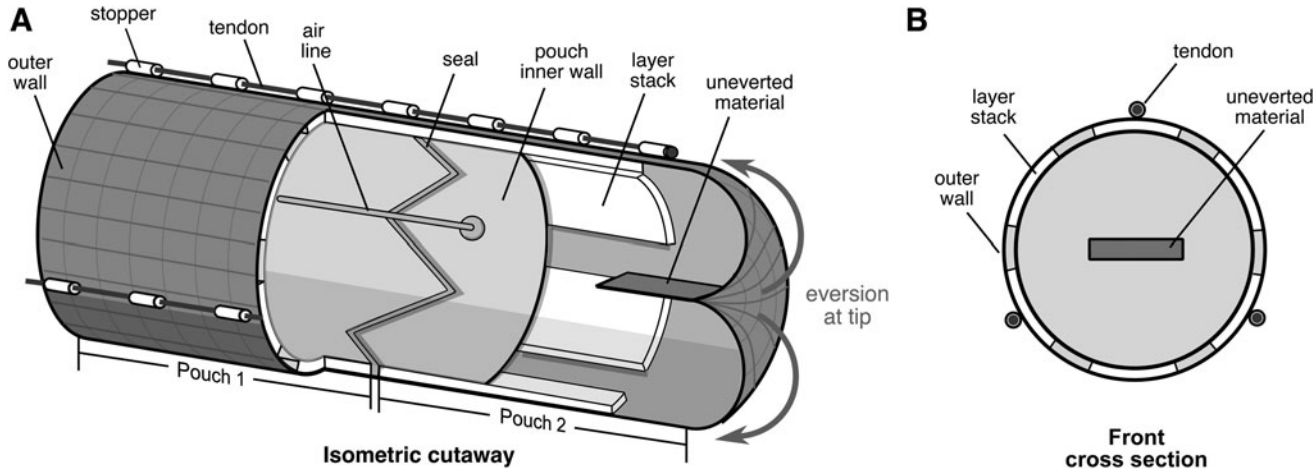


**FIG. 2.** Labeled views of the distributed discrete stiffness inflated beam robot from **(A)** an isometric cutaway perspective and **(B)** from a front cross section.

Fabrication. Figure 3 shows the step-by-step fabrication process for the robot.

The body of the inflated beam robot is a 55 mm diameter tube fabricated from flat sheets of 70 denier ripstop nylon (Quest Outfitters, Sarasota, FL, USA) with an airtight thermoplastic polyurethane (TPU) coating.

Layers are 0.1 mm thick sheets of copy paper (Amazon Basics Multipurpose Copy Paper) cut using a laser cutter (Universal Laser Systems, Inc., Scottsdale, AZ, USA) into thin strips. Paper was chosen as the layer material due to its low thickness, consistent surface frictional properties, and low cost.

To facilitate eversion of the layers, the layer width was set at 18 mm, leaving a 10.8 mm gap between adjacent layer stacks. As the robot is growing, uneverted material must transform from a flat folded state into a curved surface as it forms the beam wall. This necessitates a change in the Gaussian curvature of the material. From Gauss's *Theorema egregium*, this would not be possible for a single inextensible sheet without wrinkling or creasing.[34] The gaps between layer stacks allow the fabric to crease instead of the layers; the robot thus everts without distorting the layers. The lengths of strips is set by the desired length of each section.

Layer stacks are assembled from 15 layers and secured to the fabric using cyanoacrylate glue. A second sheet of ripstop nylon was then overlaid onto the layer stacks to form the pouch inner wall. A 3.175 mm diameter plastic tube was inserted through the inner wall for each pouch and secured in place using hot glue. Afterward, pouches were sealed using an ultrasonic welder (Vetron Typical GmbH, Kaiserslautern, Germany).

In previous study, we demonstrated a reconfigurable inflated beam robot with embedded 3D printed bistate valves.[25] Although embedding passive valves simplifies fabrication for robots with many sections, for shorter robots, the benefits of direct pouch pressure control, such as reduced response time, can outweigh its costs.

The tube is formed by folding the fabric onto its itself lengthwise and sealing along the entire length using the ultrasonic welder. The end of the tube is also sealed.

A bend is created in an inflated beam robot by applying a compressive force at the tip or through distributed loading

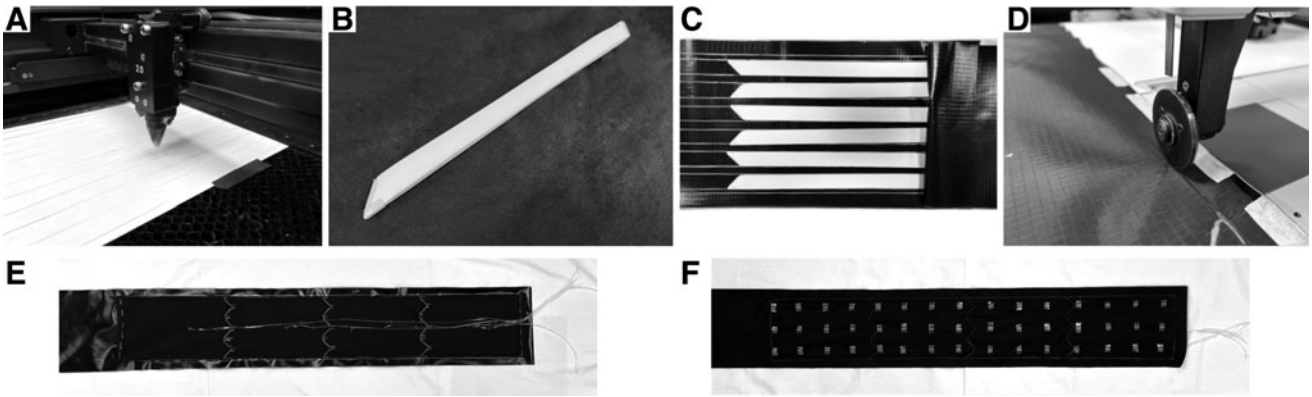


**FIG. 3.** Fabrication process for the stiffening vine robot. **(A)** Layers are first cut from copy office paper using a laser cutter. **(B)** These are assembled into layer stacks. **(C)** Six layer stacks are secured onto TPU-coated 70D-ripstop nylon fabric. **(D)** Pouches are formed by sealing the fabric using an ultrasonic welder. **(E)** Overhead view of inner vine skin before sealing, with tubes embedded into each pouch. **(F)** Overhead view of outer vine skin before sealing, with stoppers aligned along three lines. TPU, thermoplastic polyurethane.

along a side. We use tendons and stoppers to induce distributed shortening.[35] 1 cm long and 5 mm diameter polytetrafluoroethylene (PTFE) stoppers were secured using double-sided tape onto the beam outer wall with 6 cm spacing between adjacent stoppers. Spectra cables were then inserted through the stoppers. One end of the cables is secured to the tube end and the other is attached to the motorized spools. The tube is then inverted, with one end attached to the opening in the base and the other end wrapped around a spool for storage.

### *Joint design for actuation*

The interface between adjacent sections is a triangular wave to prevent premature beam buckling. There are three triangles around the beam circumference with each triangle composed of two parallelogram-shaped paper layer stacks.

The triangular wave interface prevents premature beam buckling by inhibiting the formation of wrinkles in a circular arc around the beam. When inflated beams are exposed to a bending moment, behavior is first defined by global beam bending. As the applied load is increased, local wrinkles form and begin to propagate around its circumference, eventually reaching a failure point at which point, a sharp local kink forms.[8] If the interface between adjacent sections was straight, then these wrinkles could form in the gap between layer stacks without being impeded. The triangular wave interface ensures that wrinkling must involve the jamming skin. Adjacent sections are sealed as close together as possible to minimize the area not covered by the jamming skin.

The robot bends at the interfaces between sections, and thus the interfaces act as temporary revolute joints when actuated by the tendons and stoppers. The tendons provide a force to the robot tip, and each is actuated by a motorized spool located at the robot base. Pulling on a tendon shortens that side of the robot, causing the robot to bend in that direction. Stoppers along the robot's length route the tendons axially. Three tendons are arranged radially around the center of the cross section, 120° from each other, enabling bending in 3D free space.

### *Robot system*

Figure 1B shows the full robot system. The end of the robot body, described in Body Design for Activation section, is attached to an opening in a rigid pressure vessel. The body is then inverted and stored on a spool inside the pressure vessel. This forms the robot base. The robot body grows when the base is pressurized. Motorized spools are secured at the front of the robot for actuation.

## Stiffness Characterization

The bending behavior of an inflated beam robot depends on its stiffness. We characterized the material stiffness, beam stiffness, and joint stiffness using empirical tests and finite element analysis (FEA) for our inflated beam robot.

### *Material stiffness*

We obtained material parameters for FEA by conducting three-point bending tests using an Instron universal test machine (Model 3344; Instron, Norwood, MA, USA) on an individual stack of 15 layers of copy paper (Fig. 4A). The

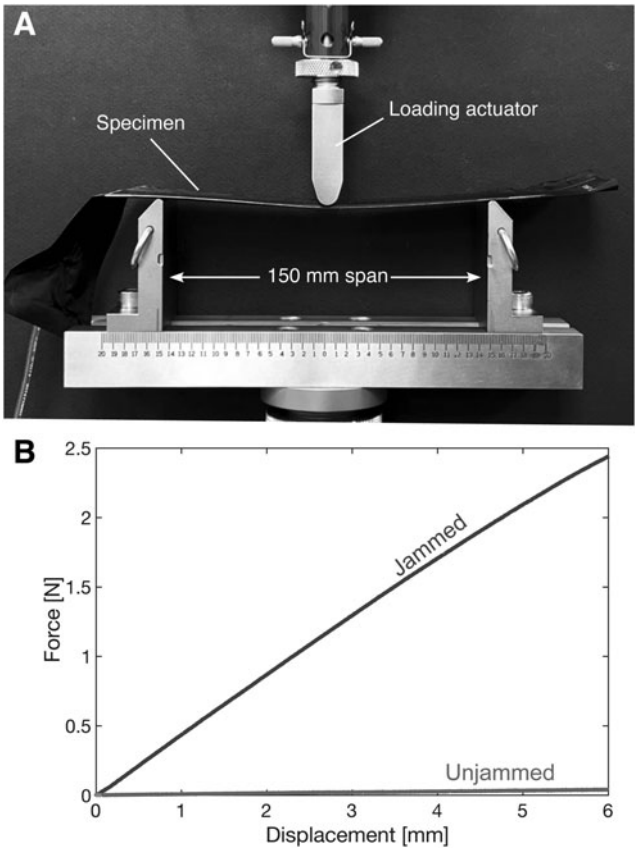


**FIG. 4.** Materials characterization. **(A)** Three-point bending test setup. **(B)** Force–displacement curves for stack of 15 layers. For the jammed and unjammed conditions, force curves remain consistent across displacements tested.

layers with a width $b$ of 35 mm were sealed inside the same TPU-coated ripstop nylon described in Fabrication section, resulting in a total thickness $d$ of 1.82 mm. A beam span $L$ of 150 mm was used.

The beam, unjammed or jammed at vacuum pressure, was displaced to 6 mm at a rate of 24 mm/min. Figure 4B shows the force–displacement curves of two tests. The flexural modulus is calculated by $E = (L^3 m)/(4bd^3)$, where $m$ is the slope from the initial portion (displacement <0.5 mm) of the force–displacement curve. The effective material stiffness from the flexural modulus of the unjammed and jammed states are calculated to be 263.2 and 3038.6 kPa, respectively.

### *Beam stiffness change due to jamming*

To characterize the effect of jamming skins on the buckling of inflated beam robots, we tested the bending stiffness of a 55 mm diameter, 250 mm long inflated beam with a single jamming section of 6 layer stacks, each composed of 15 layers of copy paper, running along the beam's length.

Figure 5A shows the test setup used to measure the bulk beam stiffness. A clamp secured one end of the inflated beam. A 3D-printed attachment on a Mark-10 Series 5 force gauge applied a transverse force to the other end of the beam. The force gauge was mounted on a motorized linear rail traveling at 0.2 mm/s for a tip deflection of 10 mm. We measured force–displacement curves for three sets of beam internal pressures—6.9, 13.8, and 20.7 kPa (1, 2, and 3 psi) gauge—

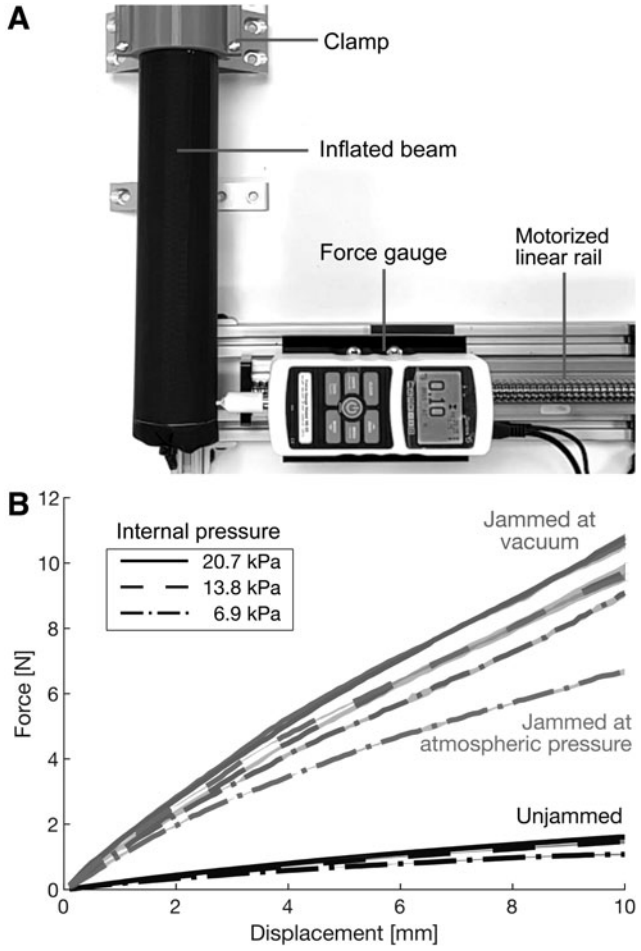


**FIG. 5.** Jamming skins allow beam stiffness to be tuned. **(A)** Test setup for beam transverse loading using a force gauge on a motorized linear rail. **(B)** Beam stiffness increases modestly with beam internal pressure and significantly with jamming. *Shaded regions* represent one standard deviation. *Solid colored lines* represent the mean.

and three sets of pouch pressure differences—jammed at vacuum, jammed at atmospheric pressure (pouch pressure at atmospheric pressure), and unjammed (pouch pressure at internal pressure).

Therefore, for example, for a 6.9 kPa internal pressure, jamming at atmospheric pressure corresponds to a $\Delta P = 6.9$ kPa with the pouch pressure, whereas for a 20.7 kPa internal pressure, it corresponds to a $\Delta P = 20.7$ kPa. Five trials were recorded for each of the nine conditions.

Figure 5B shows the force–displacement curves. Across conditions, increasing the internal pressure increased the beam stiffness, with diminishing returns on stiffness increase due to the layers providing most of the stiffness. For the unjammed case, increasing internal pressure produces relatively modest stiffness change. In contrast, jamming the layers produces a large increase in stiffness. For a 6.9 kPa internal pressure the unjammed beam requires 1.07 N to displace 10 mm, whereas the beam jammed at atmospheric pressure requires 6.68 N—a 624% increase. For a 20.7 kPa internal pressure, the force increases 663%. Jamming enables stiffness change otherwise only possible with very high internal pressure.

There is also a diminishing return to the stiffness change with an increase in the pouch pressure difference. For internal pressures of 13.8 and 20.7 kPa, the mean percentage difference between jamming at atmospheric pressure and at vacuum are 4.7% and 2.1%, respectively. This is possibly due to the bulk stiffness of the jammed layers being the limiting factor rather than the layers delaminating due to insufficient friction force. The comparable performance indicates that positive pressure jamming is an effective means for varying stiffness and that a negative pressure source is not required.

### *Joint stiffness*

Figure 6A shows the experimental setup for the joint stiffness characterization tests. An inflated beam was fabricated with two independently jamming pouches. A transverse load was applied using the same experimental setup as for the single segment tests as shown in Figure 5A. For these tests, the tip displacement was precisely controlled using the motorized track and the resulting force measured by the force gauge. Reflective marker patterns were used to measure the orientation of the front and back segments of the inflated beam using an OptiTrack motion capture camera system with Flex 13 cameras.

By modifying the bending stiffness of the joint, the bending location of the beam is controlled. Figure 6B shows how the joint stiffness affects the bending behavior of the beam. When the segment distal to the base is unjammed, a joint forms at the interface between the proximal and distal segments, resulting in the proximal segment remaining undisturbed, whereas the distal segment bends. When both segments are jammed, the joint stiffness increases and the beam bends as a single unit at its base.

FEA simulations of the two-segment tube with independently tunable stiffness are carried out using ABAQUS 2021 (Dassault Systèmes, France), as shown in Figure 6C. Linear elastic models are used with effective Young's moduli of 263.2 and 3038.6 kPa for the unjammed and jammed regions, respectively, and the same Poisson's ratio of 0.45. Consistent with the experimental results, localized buckling occurs between the two segments of the tube under a transverse load when only the distal segment is unjammed. In contrast, when both segments are jammed, the tube shows no obvious relative rotation between the two segments but deforms mainly at the fixed end of the tube, which agrees well with the experimental results.

Figure 6D shows an overlay of the body segment angles over time as well as the applied force producing this change from the empirical testing. The difference in joint bending behavior is seen by comparing the distal segment angle $\theta_1$ and proximal segment angle $\theta_2$ between the unjammed and jammed cases. When the distal segment is unjammed, the tip deflection is primarily due to the rotation of the distal segment, whereas when the distal segment is jammed, the entire structure behaves as a single unit, with the distal and proximal angles tracking together.

### *Payload capacity*

The maximum tip payload for the robot is a function of its body configuration (link lengths and joint angles), internal pressure, and jamming pressures of its external pouches. Depending on these parameters, there is a range of possible

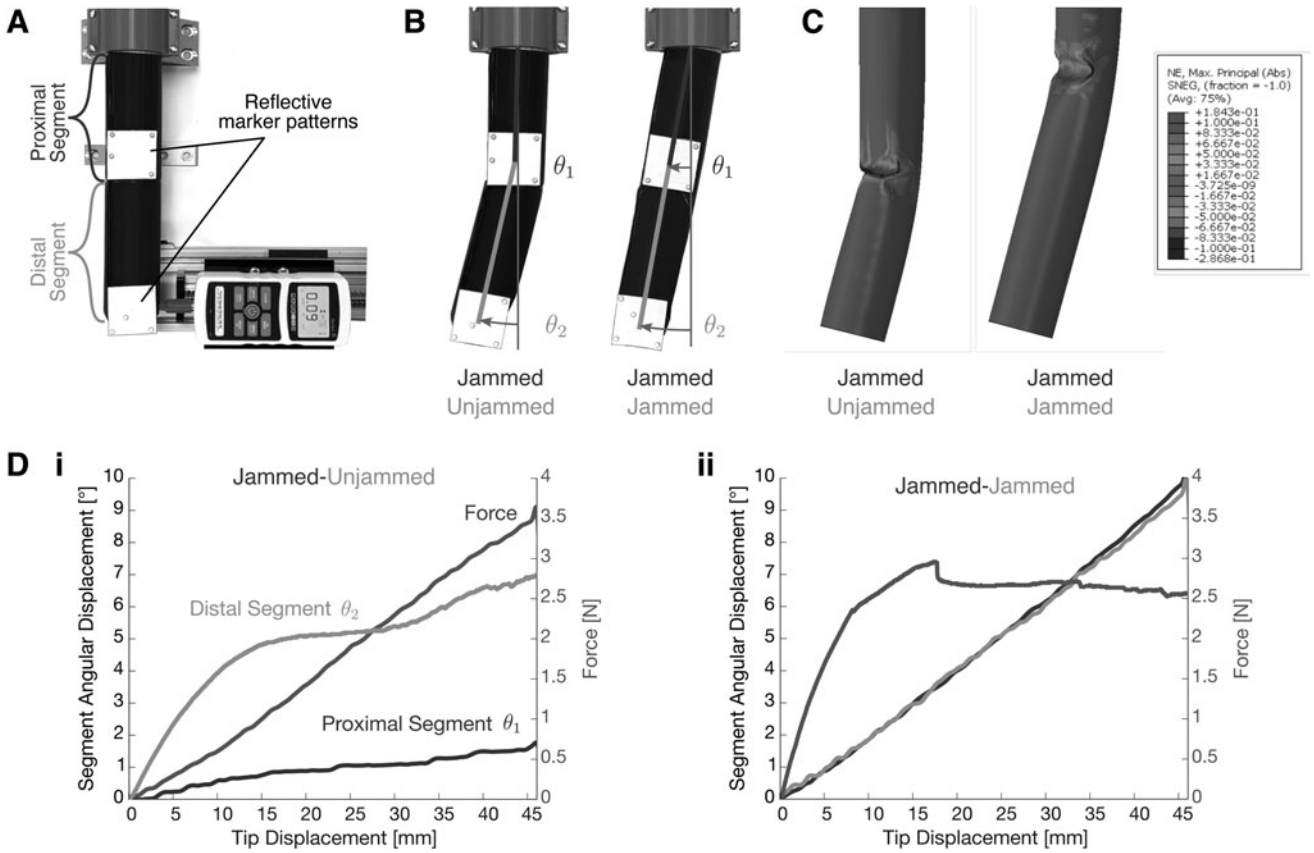


**FIG. 6.** Bending tests with a two-segment stiffening inflated beam robot. **(A)** Test setup for beam transverse loading. Retroreflective markers are placed at the end of each segment to allow measurement of position and orientation using a motion capture system (not pictured). **(B)** (i) When the proximal segment is jammed whereas the distal segment is unjammed, the boundary between the two acts as a pivot. (ii) Jamming both sections results in the entire beam behaving cohesively. **(C)** FEA depicts the same pattern of bending. Here, strain is shown. **(D)** When the distal segment is unjammed and the proximal is jammed, the distal has a larger angular displacement. When both are jammed, the two have the same angular-displacement curves. (i) Applied transverse force at the tip increases monotonically due to the restoring torque from the bent beam. (ii) Force increases linearly then plateaus due to the formation of a crease in the robot's proximal section. FEA, finite element analysis.



maximum tip payloads for the robot. We focus on the case that results in the lowest maximum payload and outline how to estimate payload for other cases. For simplicity, we neglect the effect of the tendons, which can provide additional stiffness through antagonistic actuation with the robot internal pressure.[11,36] Therefore, our analysis represents a conservative estimate for the robot's maximum tip payload.

In the case of a completely unjammed robot, the robot's behavior is comparable with that of thin-walled inflated beam. Therefore, we follow a similar approach used by McFarland and Coad to calculate the collapse of soft growing inflated beam robots.[37] For a robot in a given configuration and a payload applied to its tip, the weight of that payload can be decomposed into axial and transverse forces that act parallel and perpendicular to the axes of the robot's links, respectively.

There are four main ways that the inflated beam robot could fail given a tip payload: (1) buckling from transverse forces, (2) buckling from compressive axial forces, (3) crushing from compressive axial forces, and (4) material yielding from tensile axial forces. Because of the high ratio of length to radius and high material yield strength, we ignore cases 3 and 4, respectively. Therefore, to determine the maximum payload, we calculate the expected critical buckling force using the equations for transverse and axial buckling and then select the lower force value as the maximum payload.

For the transverse case, Comer and Levy[14] calculated the critical collapse moment $M_{\text{collapse}}$ for an inflated beam with negligible weight. However, McFarland and Coad showed that the weight of the robot body $F_{\text{weight}} = mg$ is also important to consider for real systems.[37] Therefore, we calculate the critical transverse force $F_{\text{tr}}$ required for collapse as

$$F_{\text{tr}}L = M_{\text{collapse}} - M_{\text{weight}} = \pi PR^3 - mg\frac{L}{2}, \qquad (1)$$

where $L$ is the unsupported beam length, $M_{\text{weight}}$ is the moment due to the robot's weight, $P$ is the internal pressure, and $R$ is the beam radius. Here, we assume $R << L$ in calculating $M_{\text{weight}}$. Note that for a sufficiently large $L$, $M_{\text{weight}} = M_{\text{collapse}}$ and thus, $F_{\text{tr}} = 0$.

For the axial compressive case, using the Fichter model for axial buckling[38] and taking into account the weight:

$$F_{ax} = F_{buckle} - F_{weight} = \frac{EI\frac{\pi^2}{L^2}(PA + G\pi Rt)}{EI\frac{\pi^2}{L^2} + PA + G\pi Rt} - mg, \quad (2)$$

where $F_{ax}$ is the axial force required for collapse; $F_{buckle}$ is the critical force for axial buckling for a beam of negligible weight; $E$, $G$, and $t$ are Young's modulus, shear modulus, and thickness of the wall material, respectively; $I$ is the beam second moment of area; and $A$ is the cross-sectional area.

Across different configurations, the lower bound on maximum tip payload arises when transverse buckling occurs.[37] In comparison, failure due to axial buckling requires higher forces. Therefore, the set of parameters that will produce the lowest maximum tip payload is that of a cantilevered unjammed robot at a low internal pressure. In contrast, the set of parameters that will produce the highest maximum payload is if the robot is hanging downward completely vertically, jammed, at a high internal pressure. We investigate the former case.

Consider the robot shown in Figure 8. To determine the lowest maximum tip payload, we tested the robot when cantilevered, unjammed, and at an internal pressure of 10 kPa. For this case, the unsupported length $L$ between the tip and the point of buckling is $\sim$75 cm. This is consistent with a robot weight of $\sim$175 g. Using the length to which the cantilevered robot grows before undergoing transverse buckling, we use Equation (1) to calculate what $F_{tr}$ is across a range of $L$. Note that these values for $F_{tr}$ represent a lower bound to the tip payload.

For the case of a jammed robot, the robot has a higher maximum tip payload. For a multijointed robot, the failure point will be at the joints, since the joint stiffness is less than the bending stiffness of a body segment. Therefore, $M_{collapse}$ is determined by the joint bending stiffness rather than $\pi PR^3$. We can use force–displacement tests such as those shown in Figure 6D (ii) to calculate the joint stiffness.

In the case of a multijointed robot with multiple bends, we use the joint bending stiffness to calculate the collapse moment for each joint. We then use the geometry of the current robot configuration to calculate the tip force required for each joint to reach its collapse moment. From these, the lowest tip force sets the maximum tip payload that can be achieved for that robot configuration. For example, consider a jammed multijointed vine robot composed of four 0.25 m long segments and thus three joints, as shown in Figure 8A.

Suppose that the robot is hanging downward, has grown to a length of 1 m, and has a 45° bend occurring 0.5 m down the length, similar to that shown in Figure 7D. The jammed bent joint will have a bending stiffness as shown in Figure 6C, with a peak joint resisting moment of 0.74 N·m. To estimate $F_{tr}$ for this joint, we use Equation (1) with $L = 0.5$ m and $m = 87$ g.

From this, the critical transverse tip force is $F_{tr} = 1.26$ N. Repeating this calculation for the two other joints in the robot reveals that they have higher $F_{tr}$. Therefore, the maximum tip payload is that which generates a transverse tip force of 1.26 N. For this robot configuration, the maximum tip payload weight is thus 1.8 N or 182 g. This approach can be used to estimate the maximum tip payload for any arbitrary robot configuration.

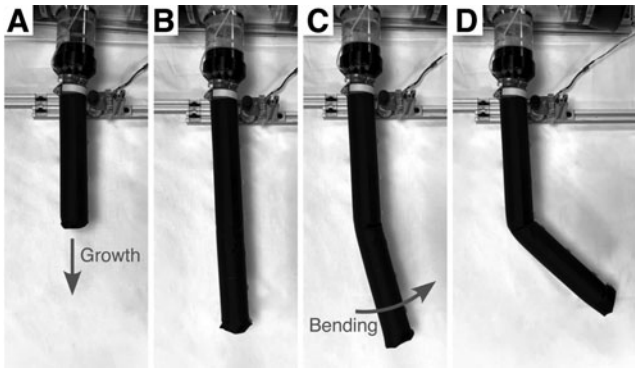


**FIG. 7.** Actuation sequence of a two-segment vine robot. **(A)** The robot grows through pressure-driven eversion to a desired length. **(B)** Once the robot reaches a desired length, a desired stiffening pattern is induced to select a pivot point and then a tendon is pulled to initiate bending. **(C)** Bending occurs about a pivot point. **(D)** The final bend configuration.

## Demonstrations: Active Shape Change and Reconfiguration

### *Growth and bending*

Our robot system achieves growth, bending, and retraction. Initially, the robot body is compactly stored on a spool in an airtight base; the body then grows to a desired length. During growth, the pouches are pressurized to the internal body pressure to ensure that the layers remain unjammed, enabling them to evert at the tip. After growth, tendons induce bending in the robot to achieve desired configurations. Figure 7 illustrates this growth and bending sequence for a two-segment vine robot.

### *Workspace*

For this demonstration, a 1 m long robot consisting of four 0.25 m long sections was fabricated. The robot was suspended from the ceiling and was actuated using three independently actuated tendons running along the length of the robot to enable motion in free space. Figure 8A shows the unactuated robot.

The addition of reconfigurable discrete joints expands the workspace of the robot. Previous study using cables to actuate everting inflated beam robots were unable to prevent buckling and had a single revolute joint at the base about which the rest of the robot pivoted.[20] Incorporating variable stiffness sections into our inflated beam robot enables us to exert compressive forces using the cables while avoiding buckling. The reconfigurable joints at the interfaces between sections can be selectively activated, enabling the robot to bend at these joints.

Figure 8 presents a time series of images showing the sequential forming and bending of temporary revolute joints. The tendon was contracted until a desired angle between adjacent segments of 30° was achieved; joint angles were measured manually using a goniometer. This configuration was generated by sequentially unstiffening and restiffening segments, starting at the most distal segment (Demonstrations: Active Shape Change and Reconfiguration section) and moving toward the base. Using a single cable, each joint can be independently actuated from the others due to the stiffness patterning.

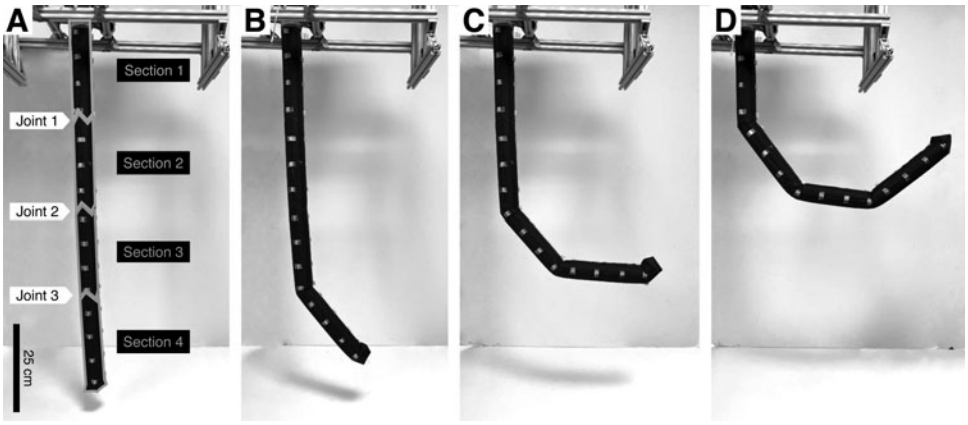


**FIG. 8.** Multibend workspace. Joints are selectively activated and bent based on the patterned stiffness. **(A)** Annotated photo showing location of each pouch and joint. Each joint can be selectively activated. **(B)** Here, the joint between Stiffness Characterization section and Demonstrations: Active Shape Change and Reconfiguration section is bent, whereas the rest of the robot remains rigid and straight. **(C)** Now, Stiffness Characterization section and Demonstrations: Active Shape Change and Reconfiguration section are stiffened, locking the bend between them in place. The joint between Materials and Methods section and Stiffness Characterization section can now be bent. **(D)** This process is repeated until all joints are bent.



For example, Figure 8B is generated by maximally jamming Introduction section, Materials and Methods section, and Stiffness Characterization section, unjamming Demonstrations: Active Shape Change and Reconfiguration section, and pulling on one of the tendons. After the desired bend angle is achieved, Demonstrations: Active Shape Change and Reconfiguration section was re-jammed, locking the bend in place during subsequent bends. This process was then repeated for Stiffness Characterization section and for Materials and Methods section.

There are several advantages of this approach compared with other state-of-the-art robots. For example, piecewise constant curvature robots require different actuation inputs for each section. Thus, generating a similar shape to that in Figure 8D would require the use of three different actuators. Although the robot configuration shown in Figure 8 could be achieved with a similarly designed global constant curvature robot with a single actuator, such a robot would suffer in its precision for targets located at a small angular displacement away from the vertical. By bringing the hinge of the joint close to the end rather than initiating bending at the robot base, we minimize the effect of actuation errors on end-effector position.

### *Multibend variable stiffness*

Varying the programmed stiffness pattern yields different output configurations from the same actuator input(s). Each joint in the robot acts as a universal revolute joint with a torsional stiffness dependent on the stiffness of its adjacent sections. The relative stiffness of these joints can be tuned by changing the pressures in each section. Given the application of a force at the tip through a tendon, the resulting displacements are determined by the relative joint stiffnesses and relative applied moment.

Figure 9 shows how three different stiffness patterns result in three different configurations. A false color overlay illustrates the pressure of each section. Figure 9A depicts the resulting configuration for a stiffness pattern that begins fully jammed at the robot base and ends fully unjammed at the

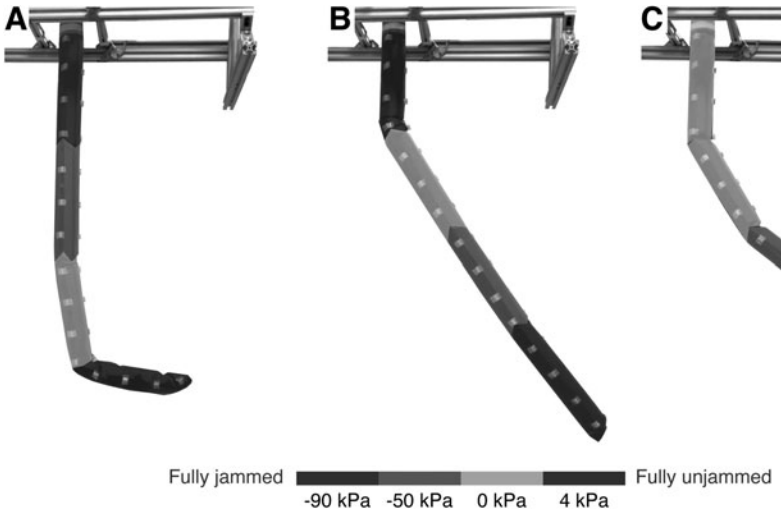


**FIG. 9.** Variable stiffness reconfiguration. The same actuator inputs yield three different output robot configurations **(A–C)**, with the location of bends determined by the patterned stiffness. A false color overlay over each robot shows the pressure in the robot skin of each section.

robot tip, whereas Figure 9B depicts the resulting configuration for the reversed stiffness pattern that begins fully unjammed at the robot base and fully jammed at the robot tip.

In Figure 9A bending occurs at both Joints 2 and 3, whereas in Figure 9B bending occurs at Joint 1 and is negligible at the other joints. Figure 9C features the same stiffness pattern as Figure 9B with the exception of Introduction section, which is now at 0 kPa, resulting in Introduction section being stiffer in Figure 9C than in Figure 9B. As a result of the more similar stiffnesses between joints, Figure 9C now features much more significant bending at Joint 2 as well as Joint 3.

### *3D shape change in free space*

Figure 1C shows two example robot configurations in free space. We actuate the robot to form shapes in free space using just three tendons that run along the entire length of the robot. Through stiffness change of the robot sections, these three tendons can independently actuate each robot joint. Each joint can be bent by pulling either an individual cable or multiple cables simultaneously and thus function similar to a 2-DOF universal joint.

## Discussion

Variable stiffness enables us to leverage an actuation-activation paradigm to decouple a vine robot's DOFs from its DOAs, thus increasing dexterity without increasing the number of actuators. By selectively varying stiffness, we activate specific DOFs on demand.

Although many existing soft robots use variable stiffness to maintain their shape in the face of external compressive forces or bending moments,[7–9,32] variable stiffness is used here to modify the effect of internal forces from the robot's actuators. That is, prior compliant systems increase their stiffness when encountering external forces to prevent excessive or undesired deformation. In contrast, our system uses stiffness to enable a handful of actuators to produce a desired deformation, yielding an output shape that is more complex than if each actuator was used to globally bend our robot.

Therefore, the pattern of stiffness, not only the magnitude of the stiffness, is an important consideration. Stiffening to selectively activate DOFs can be leveraged by many types of robots beyond inflated beam robots to enable shape change. Although pneumatic layer jamming was chosen for our robot, the use of variable stiffness for reconfiguration is generally applicable across stiffness change methods.

One direct application for our system is for steering the robot for inspection. Figures 1C, 8, and 9 all demonstrate how stiffness change enables reconfiguration in free space. In prior study, vine-like robots have been limited to exerting forces on their environment to achieve on-demand shape change.[39,40]

In addition, a variety of tip payloads such as sensors have been proposed for vine robots,[26,41,42] but these robots cannot support their weight and must rest on surfaces due to their lack of stiffness. Stiffness change addresses these issues. Furthermore, reconfiguration in free space can enable new applications such as inspection of hazardous materials, in which a robot must change shape to examine multiple locations without directly interacting with its environment.

One limitation of our current system is the use of tubing to deliver air to each jamming section. Although these flexible tubes easily accommodate the tip curvature experienced during eversion and did not substantially hinder eversion in our robot, they increase the robot skin's unjammed stiffness and eversion pressure. In general, the number of tubes (and thus jamming sections) is limited by the maximum robot operating pressure. This could be addressed by patterning air channels into the robot skin fabric[43] or embedding valves directly into each jamming pouch; we demonstrated embedding small passive valves in previous study.[25] Future study will further investigate both approaches.

Another area for future improvement is increasing the difference between the unjammed and jammed robot skin stiffnesses. Lower unjammed stiffness facilitates eversion, and higher jammed stiffness facilitates greater payload capacity. The greater the difference between these stiffnesses, the more easily bends can be formed. With layer jamming, using more layers increases both jammed and unjammed stiffness. This trade-off could be addressed using kirigami layer jamming, which involves making structured cuts into layers to reduce their second moment of area.[44]

In future study, we will develop a model for motion planning of our tendon-driven stiffening everting robot. In general, modeling tendon-driven continuum robots remains an active area of research.[45] As with other vine robots, our robot is compliant and capable of significant length change through growth. The addition of stiffening capabilities introduces discrete joints and also means that the same actuation input can yield different output shapes depending on the patterned stiffness.

Although FEA predicts the output shape of our robot, it is too computationally intensive to be used in real time and does not directly yield a generalizable model for motion planning. Leveraging the experimental characterizations presented in this article, we will develop a model capable of addressing each of these aspects of our robot for use in motion planning.

## Conclusion

This article presents the design, characterization, and fabrication of growing inflated beam robots, which leverage stiffness change to selectively activate dynamically reconfigurable discrete joints. We outline how using an actuation-activation paradigm decouples the number of controllable DOFs from DOAs and how this is realized through variable stiffness. We characterized the behavior of one- and two-segment stiffening beams experimentally and performed FEA. We also fabricated multisegment growing inflated beam robots and demonstrated how stiffness change is compatible with pressure-driven eversion, enables a larger robot workspace, yields multibend variable stiffness, and 3D shape change in free space.

The actuation-activation paradigm enabled by the selective activation of joints through stiffness change allows the mapping between actuators and the DOFs they control to be varied. A single actuator can now independently control many DOFs and the same actuator inputs can yield different shape outputs, thereby reducing the number of required actuators and simplifying active shape change. This actuation-activation paradigm could be applied across different types of soft robots to enable shape change.

Our soft robot possesses growth, variable stiffness control, and both continuum links and variable discrete joints. Future study will use our robot as a hardware platform to investigate leveraging these properties for manipulation and inspection tasks. By combining the advantages of both traditional rigid and soft manipulators, future systems could enable more collaboration between humans and robots. In addition, we would like to incorporate internal sensing to enable closed-loop control. Beyond manipulation and inspection, stiffness change across different diameter and length scales could be useful for robots in many applications, ranging from minimally invasive surgery to reconfigurable structures.

### Author Disclosure Statement

No competing financial interests exist.

### Funding Information

This study was supported in part by the National Science Foundation Graduate Research Fellowship Program; National Science Foundation grants 2024247 and 2145601; the U.S. Department of Energy, National Nuclear Security Administration, Office of Defense Nuclear Nonproliferation Research and Development (DNN R&D) under subcontract from Lawrence Berkeley National Laboratory; and the United States Federal Bureau of Investigation contract 15F06721C0002306.



### References

1. Rus D, Tolley MT. Design, fabrication and control of soft robots. Nature 2015;521(7553):467–475.
2. Piazza C, Grioli G, Catalano MG, et al. A century of robotic hands. Annu Rev Contr Robot Autonom Syst 2019; 2(1):1–32.
3. Koren Y, Weinstein Y. Inflatable Structure. Google Patents; 1991. U.S. Patent 5,065,640.
4. Voisembert S, Mechbal N, Riwan A, et al. Design of a novel long-range inflatable robotic arm: Manufacturing and numerical evaluation of the joints and actuation. J Mech Robot 2013;5(4):045001.
5. Perrot Y, Gargiulo L, Houry M, et al. Long Reach Articulated Robots for Inspection in Hazardous Environments, Recent Developments on Robotics and Embedded Diagnostics. In: International Conference on Applied Robotics for the Power Industry; 2010; pp. 1–5.
6. Yekutieli Y, Sagiv-Zohar R, Aharonov R, et al. Dynamic model of the octopus arm. I. Biomechanics of the octopus reaching movement. J Neurophysiol 2005;94(2):1443–1458.
7. Wall V, Deimel R, Brock O. Selective Stiffening of Soft Actuators Based on Jamming. In: IEEE International Conference on Robotics and Automation. IEEE; 2015; pp. 252–257.
8. Liu Y, Wang C, Tan H, et al. The interactive bending wrinkling behaviour of inflated beams. Proc R Soc A Math Phys Eng Sci 2016;472(2193):20160504.
9. Fang B, Sun F, Wu L, et al. Multimode grasping soft gripper achieved by layer jamming structure and tendon-driven mechanism. Soft Robot 2022;9(2):233–249.
10. Narang YS, Vlassak JJ, Howe RD. Mechanically versatile soft machines through laminar jamming. Adv Funct Mater 2018;28(17):1707136.
11. Stilli A, Wurdemann HA, Althoefer K. Shrinkable, Stiffness-Controllable Soft Manipulator Based on a Bio-Inspired Antagonistic Actuation Principle. In: 2014 IEEE/RSJ International Conference on Intelligent Robots and Systems; 2014; pp. 2476–2481.
12. Do BH, Choi I, Follmer S. An all-soft variable impedance actuator enabled by embedded layer jamming. IEEE/ASME Trans Mechatron 2022;27(6):5529–5540.
13. Cianchetti M, Ranzani T, Gerboni G, et al. Soft robotics technologies to address shortcomings in today's minimally invasive surgery: The STIFF-FLOP approach. Soft Robot 2014;1(2):122–131.
14. Comer R, Levy S. Deflections of an inflated circular-cylindrical cantilever beam. AIAA J 1963;1(7):1652–1655.
15. Sanan S, Moidel JB, Atkeson CG. Robots with Inflatable Links. In: 2009 IEEE/RSJ International Conference on Intelligent Robots and Systems. IEEE; 2009; pp. 4331–4336.
16. Stilli A, Wurdemann HA, Althoefer K. A novel concept for safe, stiffness-controllable robot links. Soft Robot 2017; 4(1):16–22.
17. Hawkes EW, Blumenschein LH, Greer JD, et al. A soft robot that navigates its environment through growth. Sci Robot 2017;2(8):eaan3028.
18. Mishima D, Aoki T, Hirose S. Development of Pneumatically Controlled Expandable Arm for Search in the Environment with Tight Access. In: Field and Service Robotics. (Yuta S, Asama H, Prassler E, et al. eds.) Springer; 2003; pp. 509–518. Available from: https://link.springer.com/chapter/10.1007/10991459_49 [Last accessed: April 23, 2024].
19. Tsukagoshi H, Arai N, Kiryu I, et al. Tip growing actuator with the hose-like structure aiming for inspection on narrow terrain. Int J Autom Technol 2011;5(4):516–522.
20. Stroppa F, Luo M, Yoshida K, et al. Human Interface for Teleoperated Object Manipulation with a Soft Growing Robot. In: IEEE International Conference on Robotics and Automation; 2020; pp. 726–732.
21. Greer JD, Blumenschein LH, Alterovitz R, et al. Robust navigation of a soft growing robot by exploiting contact with the environment. Int J Robot Res 2020;39(14):1724–1738.
22. Abrar T, Putzu F, Ataka A, et al. Highly Manoeuvrable Eversion Robot Based on Fusion of Function with Structure. In: IEEE International Conference on Robotics and Automation. IEEE; 2021; pp. 12089–12096.
23. Der Maur PA, Djambazi B, Haberthür Y, et al. RoBoa: Construction and Evaluation of a Steerable Vine Robot for Search and Rescue Applications. In: IEEE International Conference on Soft Robotics. IEEE; 2021; pp. 15–20.
24. Exarchos I, Wang K, Do BH, et al. Task-Specific Design Optimization and Fabrication for Inflated-Beam Soft Robots with Growable Discrete Joints. In: International Conference on Robotics and Automation; 2022; pp. 7145–7151.
25. Do BH, Banashek V, Okamura AM. Dynamically Reconfigurable Discrete Distributed Stiffness for Inflated Beam Robots. In: IEEE International Conference on Robotics and Automation; 2020; pp. 9050–9056.
26. Coad MM, Thomasson RP, Blumenschein LH, et al. Retraction of soft growing robots without buckling. IEEE Robot Autom Lett 2020;5(2):2115–2122.

27. Steltz E, Mozeika A, Rembisz J, et al. Jamming as an Enabling Technology for Soft Robotics. In: Electroactive Polymer Actuators and Devices. Vol. 7642. SPIE; 2010; pp. 640–648. Available from: https://www.spiedigitallibrary.org/conference-proceedings-of-spie/7642/764225/Jamming-as-an-enabling-technology-for-soft-robotics/10.1117/12.853182.full [Last accessed: April 23, 2024].
28. Firouzeh A, Salerno M, Paik J. Stiffness control with shape memory polymer in underactuated robotic origamis. IEEE Trans Robot 2017;33(4):765–777.
29. McEvoy M, Correll N. In: (Hsieh MA, Khatib O, Kumar V. eds.) Shape Change Through Programmable Stiffness. Springer International Publishing: Cham; 2016; pp. 893–907.
30. Alambeigi F, Seifabadi R, Armand M. A Continuum Manipulator with Phase Changing Alloy. In: IEEE International Conference on Robotics and Automation; 2016; pp. 758–764.
31. Amend JR, Brown E, Rodenberg N, et al. A positive pressure universal gripper based on the jamming of granular material. IEEE Trans Robot 2012;28(2):341–350.
32. Ou J, Yao L, Tauber D, et al. jamSheets: Thin Interfaces with Tunable Stiffness Enabled by Layer Jamming. In: International Conference on Tangible, Embedded and Embodied Interaction; 2014; pp. 65–72.
33. Brancadoro M, Manti M, Tognarelli S, et al. Fiber jamming transition as a stiffening mechanism for soft robotics. Soft Robot 2020;7(6):663–674.
34. van Rees WM, Vouga E, Mahadevan L. Growth patterns for shape-shifting elastic bilayers. Proc Natl Acad Sci 2017;114(44):11597–11602.
35. Blumenschein LH, Koehler M, Usevitch NS, et al. Geometric solutions for general actuator routing on inflated-beam soft growing robots. IEEE Trans Robot 2021;38(3):1820–1840.
36. Althoefer K. Antagonistic actuation and stiffness control in soft inflatable robots. Nat Rev Mater 2018;3(6):76–77.
37. McFarland C, Coad MM. Collapse of Straight Soft Growing Inflated Beam Robots Under Their Own Weight. In: IEEE International Conference on Soft Robotics. IEEE; 2023; pp. 1–8.
38. Fichter W. A Theory for Inflated Thin-Wall Cylindrical Beams. Vol. 3466. National Aeronautics and Space Administration: Washington, DC; 1966.
39. Wooten M, Frazelle C, Walker ID, et al. Exploration and Inspection with Vine-Inspired Continuum Robots. In: IEEE International Conference on Robotics and Automation. IEEE; 2018; pp. 5526–5533.
40. Blumenschein LH, Coad MM, Haggerty DA, et al. Design, modeling, control, and application of everting vine robots. Front Robot AI 2020;7:548266.
41. Haggerty DA, Naclerio ND, Hawkes EW. Hybrid vine robot with internal steering-reeling mechanism enhances system-level capabilities. IEEE Robot Autom Lett 2021;6(3):5437–5444.
42. Jeong SG, Coad MM, Blumenschein LH, et al. A Tip Mount for Transporting Sensors and Tools Using Soft Growing Robots. In: 2020 IEEE/RSJ International Conference on Intelligent Robots and Systems (IROS). IEEE; 2020; pp. 8781–8788.
43. Kübler AM, Rivera SU, Raphael FB, et al. A Multi-Segment, Soft Growing Robot with Selective Steering. In: IEEE International Conference on Soft Robotics. IEEE; 2023; pp. 1–7.
44. Baines R, Yang B, Ramirez LA, et al. Kirigami layer jamming. Extr Mech Lett 2023;64:102084.
45. Rao P, Peyron Q, Lilge S, et al. How to model tendon-driven continuum robots and benchmark modelling performance. Front Robot AI 2021;7:630245.

Address correspondence to:
*Brian H. Do*
*Department of Mechanical Engineering*
*Stanford University*
*Stanford, CA 94305*
*USA*

*E-mail:* brian.do@oregonstate.edu